PAPER

Check for updates

Room-temperature sodium–sulfur battery performance with a multifunctional MoS$_2$–SiC–sulfur composite cathode

Manal Bin Zaima,[a] Osama Ragab,[b] Heba Y. Zahran,[c] Ibrahim S. Yahia,[c] Hongcai Gao,[d] M. M. El-Desoky [e] and Eslam Sheha [*b]

Room-temperature sodium–sulfur (RT Na–S) batteries are attractive low-cost energy-storage systems but remain limited by severe polysulfide shuttling, sluggish redox kinetics, and poor cycling stability. Herein, a multifunctional Mo@Si@S composite cathode is developed to regulate polysulfide chemistry and enhance electrochemical performance. The synergistic integration of polar, catalytically active MoS$_2$ and mechanically robust SiC suppresses Na$_2$S$_x$ dissolution, improves charge-transfer kinetics, and promotes diffusion-controlled Na$^+$ transport. The Na‖NaPF$_6$‖Mo@Si@S cell delivers a high initial discharge capacity of ~1400 mAh g^{-1} at room temperature and exhibits improved cycling stability after short-term ambient storage, indicating favorable electrode–electrolyte interfacial evolution. Nevertheless, pronounced capacity decay during the early cycles and limited long-term capacity retention reveal persistent challenges related to sulfur utilization and interfacial degradation. These results demonstrate both the promise and the remaining limitations of MoS$_2$–SiC-based cathodes and provide guidance for further optimization toward durable RT Na–S batteries.

Introduction

Room-temperature sodium–sulfur (RT Na–S) batteries have attracted growing attention as promising alternatives to lithium-based systems due to the abundance, low cost, and environmental friendliness of sodium resources, coupled with a high theoretical energy density of 1672 mAh g^{-1}.[1] However, despite their advantages, RT Na–S batteries still suffer from severe polysulfide dissolution, sluggish redox kinetics, and poor cycling stability, which limit their practical applications.[23] Numerous strategies have been explored to mitigate these issues, including the use of polar host materials, catalytically active additives, and structural confinement approaches. For instance, amorphous SiO$_2$ hosts can strongly interact with sodium polysulfides *via* Na–O bonding, leading to long cycle life and excellent retention even after 1460 cycles.[1] Similarly, electrocatalytic frameworks such as Fe(CN)$_6^{4-}$-doped polypyrrole or Fe$_3$S$_4$-based composites have been shown to

accelerate Na$_2$S$_n$ conversion and improve ionic-electronic conductivity in both liquid and solid-state Na–S systems.[3,4] Moreover, engineering polar sulfide catalysts like MoS$_2$ has proven to be an effective strategy for anchoring soluble intermediates and promoting rapid redox reactions, as demonstrated in defect-rich MoS$_{2-x}$ and hollow-carbon hybrid architectures that enhance Na$^+$ transport and suppress the shuttle effect.[2] At the same time, polymer binders and interfacial modifiers have been employed to reinforce electrode stability; for example, hydrogen-bonding PAA–SPAN cathodes exhibit improved adhesion, ionic mobility, and long-term cycling durability.[5] Despite these advancements, achieving a balance between chemical anchoring strength, catalytic activity, and mechanical robustness remains challenging. Localized high-concentration electrolytes (LHCE) combined with pre-sodiated activated carbon cloth anodes have been shown to suppress polysulfide shuttling, promote solid–solid conversion reactions, and enhance electrode stability, achieving high coulombic efficiencies and extended cycling performance.[6,7] The addition of molybdenum disulfide (MoS$_2$) to sulfur cathodes is considered an effective strategy to suppress polysulfide shuttling in sodium–sulfur batteries. MoS$_2$ possesses high polarity and strong catalytic activity, which helps to anchor polysulfides through strong polar interactions, thereby reducing their dissolution and migration into the electrolyte.[8,9] Furthermore, using MoS$_2$ nanosheets anchored on N,O-codoped carbon improves electronic conductivity and enhances catalytic activity by increasing the Lewis acidity of

[a] General Sciences Department, College of Applied Sciences, AlMaarefa University, Diriyah, 13713, Riyadh, Saudi Arabia

[b] Physics Department, Faculty of Science, Benha University, Benha, 13518, Egypt. E-mail: islam.shihah@fsc.bu.edu.eg

[c] Laboratory of Nano-Smart Materials for Science and Technology (LNSMST), Department of Physics, Faculty of Science, King Khalid University, P. O. Box 9004, Abha, Saudi Arabia

[d] School of Materials Science & Engineering, Beijing Institute of Technology, Beijing 100081, PR China

[e] Physics Department, Faculty of Science, Suez University, Suez, 43518, Egypt

MoS_2, accelerating the chemical transformations of polysulfides and reducing the loss of active material.[10] Additionally, spectroscopic analyses revealed that the presence of MoS_2 stabilizes intermediate species such as Na_2S_4 and Na_2S_6 and decreases the formation of $S_3^{.-}$ radicals, which contribute to sulfur loss. Thanks to these effects, incorporating MoS_2 enhances cycling performance, prolongs battery life, and reduces capacity loss associated with the shuttling phenomenon.[11,12] The addition of penta-SiC_2 (p-SiC_2) to the sulfur cathode is considered a promising strategy to enhance the performance of lithium–sulfur (Li–S) batteries by suppressing the polysulfide shuttling phenomenon, which represents one of the main challenges facing this type of battery. Density Functional Theory (DFT) calculations revealed that p-SiC_2 exhibits moderate binding energies with soluble Li_2S_n species, enabling it to effectively anchor these intermediates and prevent their dissolution into the electrolyte.[13] p-SiC_2 acts as a charge acceptor, enhancing its anchoring capability and reducing the loss of active material during charge and discharge cycles. Furthermore, it helps maintain the structural integrity of Li_2S_n compounds and minimizes their decomposition, which is crucial for preserving the efficiency and lifespan of the battery. Gibbs free energy analyses also indicated that the reduction from Li_2S_2 to Li_2S the rate-determining step can be facilitated by the presence of p-SiC_2, supporting more efficient redox reactions. Therefore, p-SiC_2 serves as an effective additive that balances binding strength with structural preservation of sulfur species, significantly improving the electrochemical performance of lithium–sulfur batteries.[14] Building on these advancements, the present study investigates the electrochemical performance of Na–S batteries, focusing on electrode structure optimization and electrolyte engineering to enhance stability, capacity retention, and overall battery safety. Together, S, MoS_2, and SiC create a multifunctional cathode architecture that combines strong polysulfide anchoring, improved conductivity, and catalytic activity, ultimately leading to higher coulombic efficiency, enhanced cycling stability, and safer, longer-lasting Na–S batteries.[15,16] By combining these complementary functions, the Mo@Si@S composite can effectively suppress the shuttle effect, enhance redox kinetics, and maintain structural integrity-thereby addressing the persistent performance bottlenecks of room-temperature Na–S batteries.

Experimental techniques

The composition of the MoS_2–SiC–S composite cathode (30 wt% sulfur, 20 wt% SiC, 20 wt% MoS_2, and 30 wt% Super P carbon) was selected based on our previous systematic study on MoS_2–SiC-based cathodes for alkali-metal battery applications.[17] The Mo@Si@S cathode was synthesized through the following procedure: a mixture comprising 30 wt% Super P carbon (MTI), 30 wt% sulfur powder (Alfa Aesar, 99%), 20 wt% silicon carbide (ALDRICH, 200 mesh), and 20 wt% molybdenum(IV) sulfide (ALDRICH, 99%) was thoroughly ground in an agate mortar to achieve uniform dispersion. The homogenized mixture was then subjected to microwave irradiation at 1200 W for 10 seconds. For electrode fabrication, 0.75 g of the Mo@Si@S

composite and 0.15 g of poly(vinylidene fluoride) (PVDF, –CH_2CF_2–)$_n$ powder was dissolved in N-methyl-2-pyrrolidone (NMP) to form a viscous slurry under magnetic stirring. The slurry was uniformly coated onto a 150 mm aluminum foil substrate using a HOHSEN MC-20 Mini-Coater. Based on the composite composition (30 wt% sulfur) and electrode geometry, the resulting sulfur areal loading was approximately 1.0–1.3 mg cm^{-2}. The coated foil was dried in an oven at 100 °C for two hours. Subsequently, cathode discs with a diameter of 14 mm were punched out and stored in an incubator at 55 °C to prevent moisture absorption. CR2032-type coin cells were assembled in a domestic argon-filled glovebox. The cells consisted of a sodium (Na) metal disc as the anode, a sulfur (S)-based cathode, and a Whatman fiber glass membrane serving as the separator. The electrolyte used was 1 M $NaPF_6$ dissolved EC/PC = 1 : 1 (v/v) solution. The cathode was prepared and dried prior to cell assembly. A single piece of fiber glass separator was wetted with 0.1 ml electrolyte before being placed between the anode and cathode. The components were carefully stacked in the following order: stainless steel spacer, Na disc, fiber glass separator (electrolyte-wetted), S cathode, and another spacer, then sealed within the CR2032 coin cell casing using a crimping machine. Electrochemical characterizations were performed using a CHI604E electrochemical workstation for cyclic voltammetry (CV) and electrochemical impedance spectroscopy (EIS) measurements. Galvanostatic charge–discharge cycling was conducted using a Neware battery testing system under specified current densities (20 μA) and a cutoff voltage window (0.5 V/3.5 V). All cell assembly and electrochemical testing procedures were conducted at room temperature. XRD patterns were measured using a MiniFlex 600 diffractometer, while SEM images were obtained using a JEOL JCM-7000 microscope.

Results and discussion

Fig. 1(a) illustrates the cyclic voltammetry (CV) curves of the Na‖$NaPF_6$‖Mo@Si@S cell measured over five consecutive cycles (C1–C5) within a potential window of 0.0 to 4.0 V $vs.$ Na/Na$^+$ at room temperature. In the first cycle (C1), broad and pronounced redox peaks are observed, indicating initial electrochemical activation and the formation of solid electrolyte interphase (SEI) layers. The large peak separation and relatively higher current response in C1 suggest initial kinetic limitations and possible side reactions, such as electrolyte decomposition. From the second cycle (C2) onward, the CV curves become more stabilized, with well-defined and overlapping anodic and cathodic peaks, reflecting the improved reversibility of sodium-ion insertion/extraction and the enhanced electrochemical stability of the cathode system. The consistent peak positions across cycles (C2–C5) indicate stable redox processes, primarily associated with the stepwise conversion of sulfur species (e.g., S_8 to Na_2S_x and eventually Na_2S).[16] The suppression of peak distortion and current decay in subsequent scans highlights the beneficial effect of the MoS_2–SiC conductive framework in promoting fast charge transfer and stabilizing sulfur species. These results support the strong electrochemical durability and redox reversibility of the composite cathode, essential for long-

term sodium–sulfur battery performance. Fig. 1(b) displays the cyclic voltammetry (CV) profiles of the Na‖NaPF$_6$‖Mo@Si@S cell at different scan rates. As the scan rate increases, both the anodic and cathodic peak currents (I_P) rise systematically while maintaining a consistent redox profile. The anodic and cathodic peaks shift slightly, indicating a quasi-reversible redox behavior with increasing polarization at higher scan rates. This behavior is typical for sodium storage processes involving diffusion-controlled mechanisms. Fig. 1(c) demonstrates the peak current (I_P) *versus* the square root of the scan rate ($v^{1/2}$), producing a strong linear relationship in both anodic and cathodic directions, supporting diffusion-controlled kinetics, using the Randles–Sevcik equation:[18]

$$I_P = 2.78 \times 10^5 \times A \times C \times D_{Na^+}0.5 \times v^{0.5} \times n^{1.5}$$

where I_P is the peak current (A), A is the electrode area (1.53 cm^2), C is the concentration of Na$^+$ (1×10^{-3} mol cm^{-3}), v is the scan rate (V s^{-1}), n is the number of electrons transferred

(assumed as 1), and D_{Na^+} is the diffusion coefficient (cm^2 s^{-1}). By extracting the slope (S) from the linear fit of I_P *versus* $v^{0.5}$ of the anodic and cathodic plots, and rearranging the equation to solve for D_{Na^+}:[18,19]

$$D_{Na^+} = \left(\frac{S}{2.78 \times 10^5 \times A \times C \times n^{1.5}} \right)^2$$

The extracted slopes were 25.706 and 54.346 A (V s^{-1})$^{-1/2}$, respectively. Substituting into the equation, the calculated sodium-ion diffusion coefficients were anodic diffusion coefficient (D_a): 4.12×10^{-10} cm^2 s^{-1}; cathodic diffusion coefficient (D_c): 1.75×10^{-9} cm^2 s^{-1}. Fig. 1(d) depicts the electrochemical impedance spectroscopy (EIS) Nyquist plots of the Na‖NaPF$_6$‖Mo@Si@S cell before and after cyclic voltammetry (CV), providing insight into the interfacial resistance and ion transport behavior. The spectra feature a depressed semicircle in the high-to-mid frequency region, associated with charge transfer resistance (R_{ct}), and a linear Warburg tail in the low-
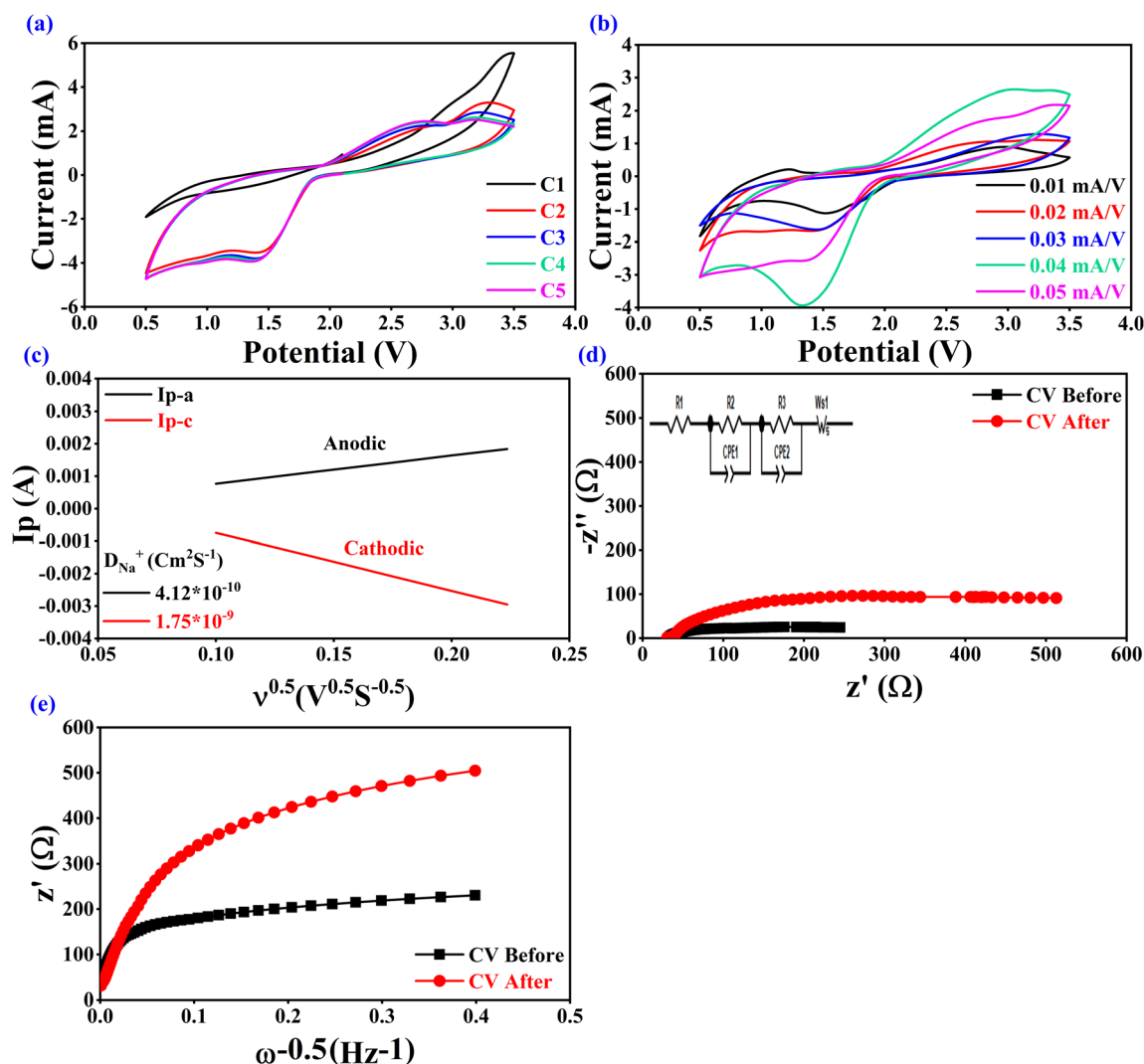

Fig. 1 (a) CV curve for the five cycles, (b) CV at different scan rate, (c) linear relationship between the current of the cathodic/anodic reaction and scan rate. (d) $-Z''$ *vs.* Z' and its equivalent circuit (inset) of Na‖NaPF$_6$‖S, (e) linear fitting ($\omega^{-0.5}$) of Warburg impedance.

Paper

frequency region, attributed to sodium-ion diffusion through the electrode matrix. Fitting the data to an equivalent circuit model (typically represented as R_s–($R_{ct}\|C_{dl}$)–W, where R_s is the solution resistance, C_{dl} the double-layer capacitance, and W the Warburg impedance) reveals that R_{ct} increases from ~203 Ω before CV to over 455.7 Ω after CV as illustrated in Table 1. This substantial rise reflects increased polarization and interfacial degradation, likely caused by the formation of resistive solid electrolyte interphase (SEI) layers or partial passivation of electrochemically active sites. The low initial impedance confirms the good intrinsic conductivity and facilitated charge transfer of the MoS$_2$–SiC framework, while the post-CV increase suggests the need for further optimization of electrolyte composition or surface modification strategies to maintain long-term electrochemical stability. Nonetheless, the retention of a Warburg-type tail even after cycling indicates that Na$^+$ diffusion remains active within the electrode, supporting the overall robustness of the composite structure. Fig. 1(d) presents the Warburg impedance plots (Z' vs. $\omega^{-1/2}$) of the Na$\|$NaPF$_6\|$□ Mo@Si@S cell before and after cyclic voltammetry (CV), which are used to evaluate the sodium-ion diffusion kinetics. In both cases, a linear relationship is observed in the low-frequency region, indicating that the ion transport is governed by semi-infinite linear diffusion. The slope of this linear segment corresponds to the Warburg coefficient (σ), which is then used to calculate the sodium-ion diffusion coefficient (D) via the equation: $D_{Na^+} = \left[\dfrac{R^2 T^2}{2A^2 n^4 F^4 C^2 \sigma^2}\right]$, where R is the gas constant (8.314 J mol^{-1} K^{-1}), T is the absolute temperature (298 K), A is the electrode area (assumed 1.0 cm^2), n is the number of electrons per reaction ($n = 2$ for Na$^+$/S conversion), F is Faraday's constant (96 485 C mol^{-1}), and C is the sodium ion concentration (estimated 1 mol cm^{-3}). The Warburg coefficients were extracted from the slopes of the linear regions at low frequencies, yielding σ before ≈ 117.6 Ω s$^{-1/2}$ and σ after ≈ 339 Ω s$^{-1/2}$. Substituting into the equation, the calculated diffusion coefficient before CV is approximately 1.08×10^{-12} cm^2 s^{-1}, while after CV it decreases to about 1.30×10^{-13} cm^2 s^{-1} as presented in Table 1. This marked decline in D_{Na^+} highlights a deterioration in sodium-ion mobility, likely due to increased charge transfer resistance and formation of anode's insulating layers during cycling. The results emphasize the importance of electrolyte optimization in maintaining ion transport efficiency over prolonged operation. The diffusion coefficients derived from cyclic voltammetry and electrochemical impedance spectroscopy differ because the two techniques probe distinct electrochemical regimes. The CV-based value reflects a large-signal, non-equilibrium process at the peak potential, whereas the EIS-based value is obtained from a small-signal, near-steady-state response and is highly sensitive to the Warburg

impedance model. In porous Na-ion electrodes, deviations from ideal semi-infinite diffusion and the dependence of Na$^+$ transport on state of charge result in method-dependent apparent diffusion coefficients rather than experimental inconsistency. Fig. 2(a and b) display the galvanostatic discharge voltage profiles of the Na$\|$NaPF$_6\|$Mo@Si@S cell at a current 20 μA over 20 successive cycles (C1–C20) at room temperature, where the capacity decreases with increased cycle number and fades after the 20 cycles (Fig. 2(c)). The cell delivers a remarkably high initial specific capacity of approximately 1400 mAh g^{-1}, with a distinct voltage plateau below 1.0 V vs. Na/Na$^+$, indicative of efficient sulfur redox reactions and effective Na$^+$ intercalation facilitated by the MoS$_2$–SiC matrix. However, a sharp decline in capacity is observed in the subsequent cycles. The voltage curves display two main discharge plateaus: an initial one around ~1.8–3.4 V and a more prominent plateau near ~0.5 V vs. Na/Na$^+$, corresponding to the stepwise reduction of sulfur into lower-order polysulfides and ultimately to Na$_2$S. Notably, the profiles remain highly consistent across cycles, indicating excellent electrochemical reversibility and structural stability of the cathode material. From cycle 3 onward, the voltage curves show minimal polarization and negligible capacity fading, reflecting stable cycling behavior. By cycle 20, the specific capacity remains above 50 mAh g^{-1}, highlighting the cathode's ability to sustain high capacity over extended use. This performance affirms the suitability of the Mo@Si@S composite for developing long-life sodium–sulfur batteries operating efficiently at room temperature. The cell was stored at room temperature for 10 days prior to cycling tests in order to assess its stability and evaluate the impact of storage on its electrochemical behavior and long-term performance. This procedure also aimed to determine whether its performance would improve or deteriorate after the storage period. Fig. 3(a–c) illustrates the cycling performance of the Na$\|$NaPF$_6\|$Mo@Si@S cell after 10 days of storage, showing the discharge capacity as a function of cycle number up to 20 cycles. At the beginning, the stored cell delivers an unusually high discharge capacity exceeding 2450 mAh g^{-1}, which is far above the theoretical capacity of sulfur (1675 mAh g^{-1}). All specific capacities reported in this work are normalized to the mass of sulfur in the cathode, with a sulfur content of 30 wt% in the MoS$_2$–SiC–S composite. The unusually high initial capacities observed in the fresh and stored cells, which exceed the theoretical capacity of sulfur (1675 mAh g^{-1}), do not originate from reversible sulfur redox reactions. Instead, they are mainly attributed to severe electrolyte decomposition and parasitic interfacial reactions at the metal anode surface during the initial cycles. These irreversible contributions lead to transient excess capacity, followed by rapid decay and stabilization at much lower values, reflecting the true electrochemical utilization of sulfur.

Table 1 EIS parameters of Na$\|$NaPF$_6\|$Mo@Si@S cell before and after cycling volumetry (CV)

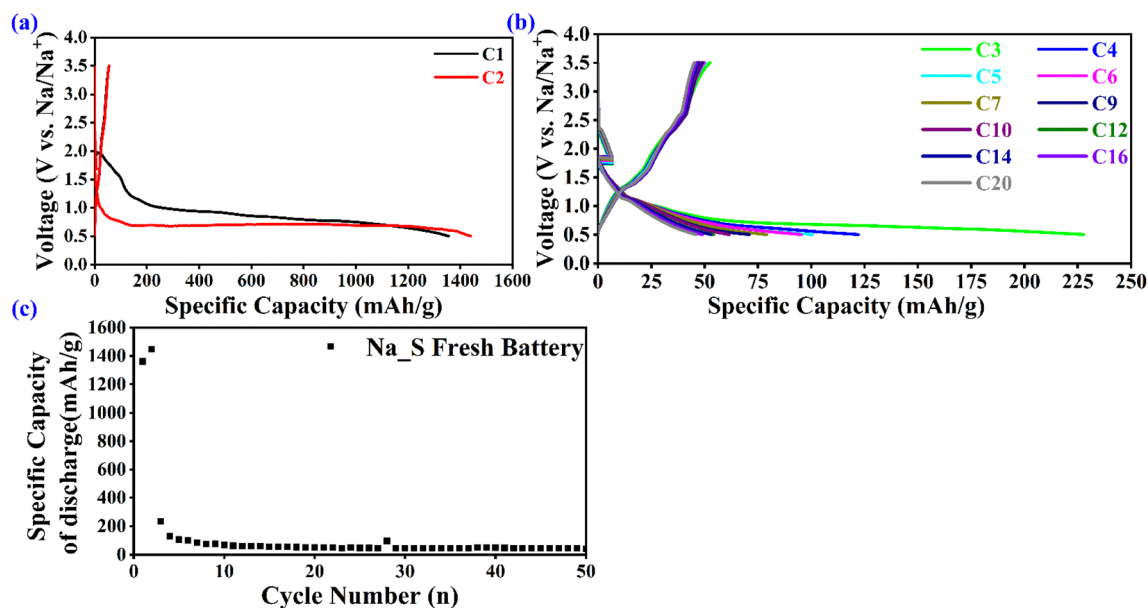| EIS parameters	R_s (Ω)	R_{SEI} (Ω)	R_{ct} (Ω)	CPE$_1$ (F)	CPE$_2$ (F)	A_w (Ω)	D (cm^2 s^{-1})
Na$\|$NaPF$_6\|$Mo@Si@S_B_CV	33.3	62.66	203.3	0.580	0.4555	117.59	1.08×10^{-12}
Na$\|$NaPF$_6\|$Mo@Si@S_A_CV	30.99	40.92	455.7	1.036	0.5091	338.95	1.30×10^{-13}

Fig. 2 (a) Specific capacity of discharge with cycle number, at 25 °C at a current 20 mA and galvanostatic discharge_charge curves of Na‖NaPF$_6$‖Mo@Si@S fresh full cell for: (b) C1 and C2; (c) from C3 to C20.
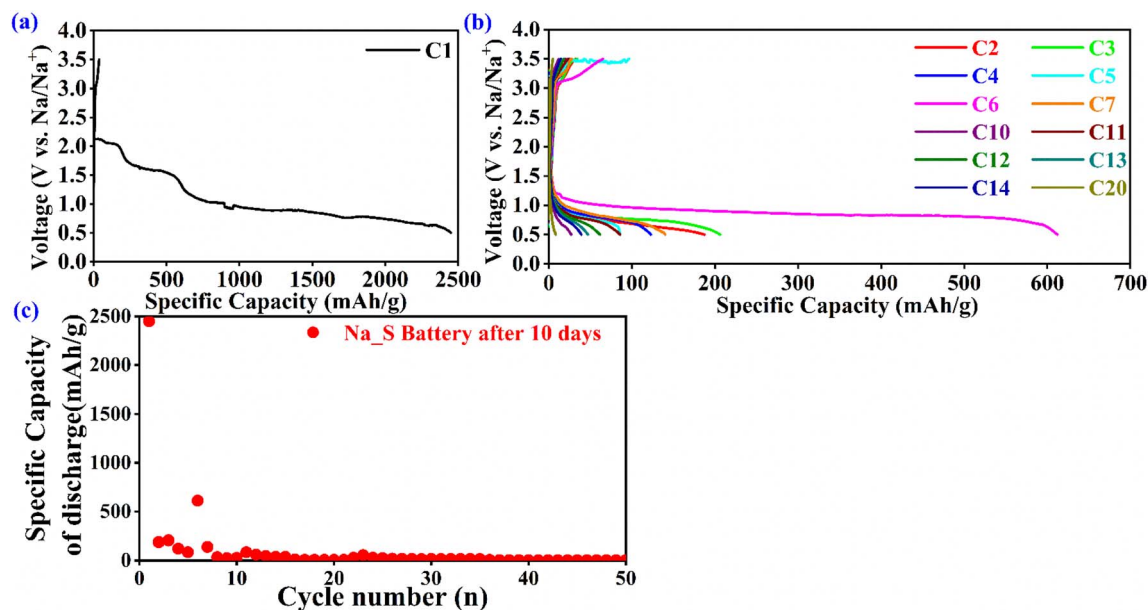

Fig. 3 After 10 days of storage (a) specific capacity of discharge with cycle number, at room temperature at a current 20 mA and galvanostatic discharge_charge curves of Na‖NaPF$_6$‖Mo@Si@S full cell after cell rest for 10 days for: (b) first cycle (C1); (c) from C2 to C20.

However, this excessive capacity rapidly decays, dropping below 200 mAh g^{-1} by the third cycle and stabilizing around 50–80 mAh g^{-1} after the tenth cycle. Such a drastic decline indicates severe capacity fading, most likely arising from the polysulfide shuttle effect, limited electronic conductivity, and irreversible formation of inactive sodium sulfides. The nearly flat capacity profile observed beyond the early cycles also reflects poor sulfur utilization and structural instability of the cathode material. Interestingly, the cell tested after 10 days of storage (Fig. 3(c)) performed more favorably than the fresh cell tested

immediately (Fig. 2(b)). The stored cell exhibited improved cycling stability and a higher discharge capacity, suggesting that the brief storage period may have facilitated beneficial electrode–electrolyte interactions or mitigated some of the parasitic reactions observed in the fresh cell. Moreover, the 10-day stored cell showed more stable voltage profiles, higher coulombic efficiency, and less capacity fading across repeated cycles, all of which indicate improved structural integrity of the sulfur cathode and enhanced reversibility of the electrochemical processes. Overall, these findings highlight that short-term

storage (10 days at room temperature) can enhance the electrochemical performance of Na–S batteries, providing a simple yet effective strategy for improving their stability and cycle life. The improved cycling stability observed after 10 days of storage is reported here as an empirical and reproducible electrochemical observation. At this stage, no definitive mechanism is assigned, as distinguishing the relative contributions of interfacial evolution, SEI/CEI stabilization, or electrolyte wetting effects would require additional dedicated analyses beyond the scope of this study. Accordingly, this effect is discussed in a phenomenological manner without asserting a specific underlying process. Fig. 4(a and b) illustrates the rate capability of the room-temperature sodium–sulfur (Na–S) battery employing a conventional sulfur cathode after 10 days of storage at room temperature. The cell was tested under stepwise current densities of 20, 40, and 60 μA, followed by a return to 20 μA. Fig. 4(c) summarizes the rate performance, where increasing the current density to 40 and 60 μA leads to a further reduction and stabilization of the discharge capacity in the range of 50–70 μAh g^{-1}, reflecting sluggish reaction kinetics and limited rate tolerance. Upon returning to 20 μA, only partial capacity recovery is observed, indicating irreversible structural and chemical degradation of the sulfur cathode during high-rate cycling. Overall, these results underscore the intrinsic limitations of conventional sulfur cathodes-namely low conductivity, severe polysulfide shuttling, and poor redox reversibility-and highlight the necessity of advanced cathode designs, such as MoS$_2$–SiC composites, to achieve stable and high-rate Na–S battery performance. The schematic diagram (Fig. 5) illustrates the proposed working principle and redox mechanism of the room-temperature sodium–sulfur (Na–S) battery employing a multifunctional MoS$_2$–SiC–S composite cathode. During discharge, sodium metal at the anode is
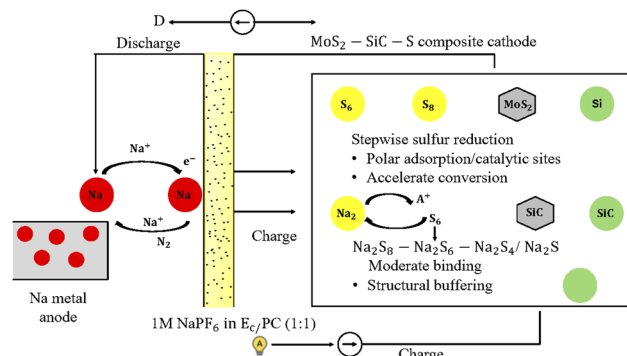

Fig. 5 Schematic of the discharge/charge mechanism of a room-temperature Na−S battery with a MoS$_2$−SiC−S composite cathode. Na metal releases Na$^+$ ions that react with sulfur (S$_8$ → Na$_2$S$_8$ → Na$_2$S$_6$ → Na$_2$S$_4$ → Na$_2$S$_2$/Na$_2$S) during discharge and revert during charge.

oxidized to Na$^+$ ions, releasing electrons that travel through the external circuit to the cathode. The Na$^+$ ions simultaneously migrate through the electrolyte (1 M NaPF$_6$ in EC/PC = 1 : 1) and react with sulfur species within the composite cathode. The reduction of sulfur proceeds stepwise from S$_8$ → Na$_2$S$_8$ → Na$_2$S$_6$ → Na$_2$S$_4$ → Na$_2$S$_2$/Na$_2$S, forming soluble polysulfides that are subsequently converted into insoluble Na$_2$S. Upon charging, the reverse reactions occur, reoxidizing Na$_2$S to elemental sulfur and regenerating Na at the anode. The incorporated MoS$_2$ nanosheets serve as polar catalytic hosts that effectively adsorb intermediate Na$_2$S$_x$ species and accelerate their redox conversion, while SiC nanoparticles provide structural buffering and moderate binding strength to polysulfides, thereby mitigating the shuttle effect and maintaining cathode integrity. Table 2 presents a comparative summary of the
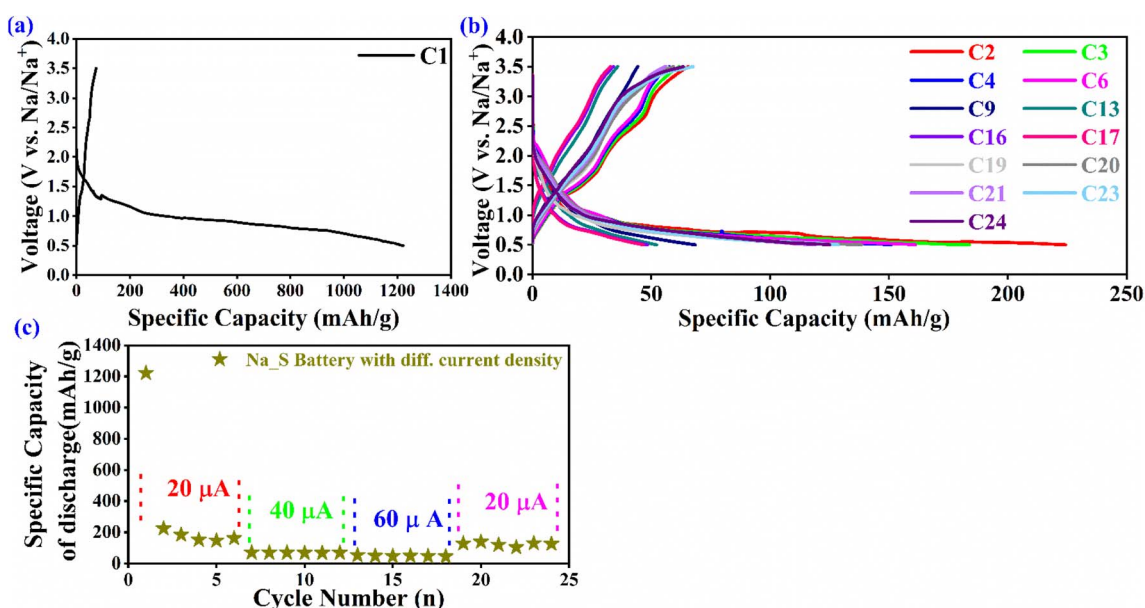

Fig. 4 (a and b) Galvanostatic discharge_charge curves of Na∥NaPF$_6$∥Mo@Si@S full cell; (c) specific capacity of discharge with cycle number, with different current rate [20 μA, 40 μA, 60 μA, 20 μA].

Table 2 Comparison of electrochemical performance parameters of various room-temperature sodium–sulfur (Na–S) batteries

Ref.	Cathode system/strategy	Sulfur loading (wt%)	Initial specific capacity (mAh g^{-1})	Rate capability (mAh g^{-1} at high current)	Cycle stability (capacity retention/cycles)	Key functional mechanism
	MoS$_2$–SiC–S composite (microwave-processed multifunctional cathode)	30	890	460	≈10% after 25 cycles (0.5 A g^{-1})	Synergistic catalytic MoS$_2$ + moderate-binding SiC suppress shuttle and accelerate Na$_2$S$_n$ redox conversion
5	SPAN + PAA binder (eco-friendly hydrogen-bonding interaction)	≈45	650	—	Stable >200 cycles (0.5C)	PAA-SPAN H-bonding enhances adhesion, ion diffusion and cathode integrity
2	Flower-like interlayer-expanded MoS$_{2-x}$ @ hollow carbon spheres	≈75	620	416	85.2% after 100 cycles	Sulfur-vacancy MoS$_{2-x}$ nanosheets + conductive carbon matrix → fast Na$^+$/e$^-$ transport and strong NaPS adsorption
4	Fe(CN)$_6^{4-}$-doped polypyrrole@carbon fiber (core–shell)	≈70	1071	700	700 mAh g^{-1} after 200 cycles	Fe redox mediators enable quasi-solid-state Na$_2$S$_4$ ↔ Na$_2$S conversion
1	Sulfur in amorphous silica (polar Si-O host)	73.5	956	940	≈100% after 1460 cycles	Na-O bonding and amorphous SiO$_2$ pores suppress shuttle and buffer expansion
3	Fe$_3$S$_4$@S @0.9Na$_3$SbS$_4$·0.1NaI (all-solid-state)	≈60	1040	446	410 mAh g^{-1} after 50 cycles	Fe$_3$S$_4$ enhances electronic conductivity; in situ Na$_3$SbS$_4$ NaI electrolyte improves ionic transport and stability

electrochemical performances of the present MoS$_2$–SiC–S composite cathode and recently reported room-temperature Na–S systems. The proposed composite delivers an initial specific capacity of 890 mAh g^{-1}, but the capacity retention decreases to about 10% after 25 cycles, indicating rapid fading during the early cycles. Despite this limitation, the result highlights the strong initial electrochemical activity achieved through the synergistic effect of polar MoS$_2$ and stable SiC, which together enhance redox kinetics and suppress the polysulfide shuttle. In comparison, the SPAN–PAA cathode shows lower initial capacity (≈ 650 mAh g^{-1}) but remarkable stability beyond 200 cycles, attributed to hydrogen-bond-reinforced interfacial cohesion. The interlayer-expanded MoS$_{2-x}$@hollow-carbon composite and Fe(CN)$_6^{4-}$-doped polypyrrole/carbon fiber electrode (ref. 4) achieve higher long-term retention (85–100 cycles) through enhanced electron/ion transport and electrocatalytic conversion of Na$_2$S$_n$ species. Meanwhile, the amorphous-silica host and Fe$_3$S$_4$@S@Na$_3$SbS$_4$ NaI solid-state system display exceptional durability-maintaining almost full capacity after 1460 and 50 cycles, respectively-because of strong chemical confinement and improved ionic conductivity. As summarized in Table 2, the present MoS$_2$–SiC–S cathode demonstrates competitive initial electrochemical activity compared with recently reported room-temperature Na–S systems, highlighting the effectiveness of combining polar catalytic MoS$_2$ with mechanically robust SiC through a simple microwave-assisted process. The main innovation of this work lies in this facile composite design, which enables rapid sulfur redox kinetics and mitigated polysulfide dissolution without complex synthesis routes. However, in contrast to systems employing strong chemical confinement or advanced electrolyte engineering, the present cathode still exhibits rapid capacity fading during early cycles, indicating insufficient long-term interfacial stabilization. These limitations identify clear improvement space, including further optimization of the composite architecture, electrolyte compatibility, and interface engineering, to translate the high initial activity observed here into more durable cycling performance. To investigate the structural and morphological evolution of the sulfur (S) cathode at different electrochemical states, cathodic samples were extracted from Na‖NaPF$_6$‖Mo@Si@S full cells. In one case, the cell was discharged to 0.5 V, while in another, it was subjected to a full discharge–charge cycle (sodiation/de-sodiation) between 0.5 and 3.5 V. The recovered cathodes were subsequently cleaned with acetonitrile (ACN) and dried at room temperature overnight. Fig. 6(a) presents the X-ray diffraction (XRD) patterns of the Mo@Si@S composite cathode in three distinct electrochemical states: pristine (S$_0$), discharged (S$_1$), and discharged/charged (S$_2$). The cathode consists of sulfur (S), molybdenum sulfide (MoS$_2$), silicon carbide (SiC), and super carbon (C). In the pristine state, the pattern reveals sharp, intense peaks in the 10°–20° range and beyond, attributed to orthorhombic sulfur (S$_8$), with dominant reflections around 22.33°, 28.73°, 35.16°, 39.24°, 43.86°, 49.54°, 59.86°, and 64.83°, corresponding to the (131), (135), (244), (424), (440), (171), (642), and (191) planes, respectively. The presence of MoS$_2$ is confirmed by peaks at 14.08°, 39.86°, 43.86°, 59.86° and 64.83°,
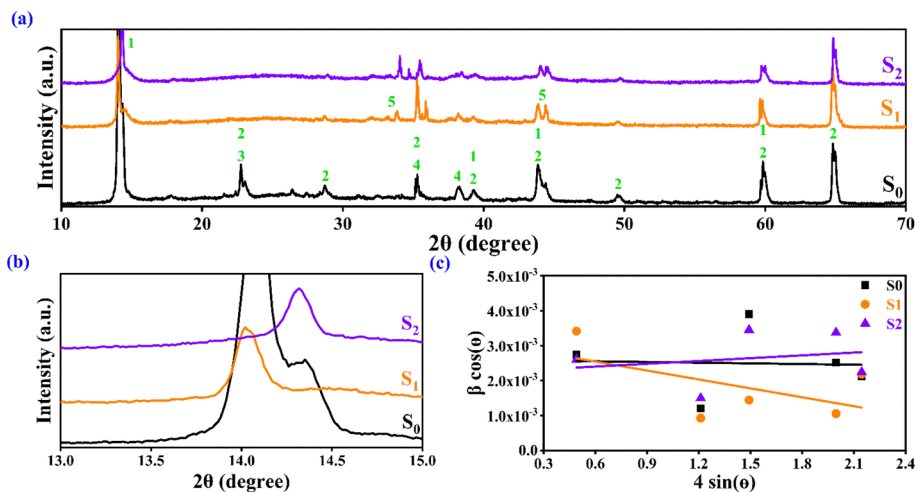
Fig. 6 (a) XRD patterns of S_0, S_1 and S_2 cathodes, (b) XRD zoomed of MoS_2 peak at $2\theta \sim 13-15°$, (c) W−H plot; 1 = MoS_2, 2 = S, 3 = C, 4 = SiC and 5 = Na_2S.

related to the (002), (104), (105), (113) and (011) planes, respectively, while carbon is appeared at peak around 22.73°, corresponding to (001) and SiC shows characteristic reflections at 35.16° and 38.19°, attributed to the (001) and (105) planes. These peaks are sharp with narrow full width at half maximum (FWHM), indicating high crystallinity, large crystallite sizes, and negligible lattice strain. Crystallite size D is estimated using the Scherrer equation: $D = \dfrac{K\lambda}{\beta \cos(\theta)}$,[20] where K is the shape factor ($\sim$0.9), λ is the X-ray wavelength (typically 0.15406 nm for Cu Kα), β is the breadth of the diffraction peak at half maximum (FWHM) in radians, and θ is the Bragg's angle. The narrow β values suggest crystallite sizes in the range of tens to hundreds of nanometers in the pristine state.

Upon discharge, the pattern exhibits significant peak broadening and intensity loss of sulfur reflections, indicating conversion of S_8 into amorphous sodium polysulfides (Na_2S_x) and crystalline Na_2S. New peaks emerge at $\sim$31° and 45° corresponding to the (211), and (222) planes, attributed to Na_2S. The broadening of these peaks and the suppression of sulfur signals indicate reduced crystallite size and increased micro strain. These microstructural changes are quantitatively analyzed using the Williamson–Hall equation

$$\beta \cos(\theta) = \frac{K\lambda}{D} + 4\varepsilon \sin(\theta)$$

where ε = the strain. Fig. 6(b) displays the magnified XRD patterns of the MoS_2 peak for the three cathodes (S_0, S_1, and S_2) that are zoomed in the $2\theta \sim 13-15°$. The variations in the diffraction peak position and strength between the three cathodes are shown in this magnified picture. A high degree of crystallinity is indicated by the strong and distinct peak seen in the pristine cathode S_0. The peak position and broadening in the S_1 and S_2 cathodes, on the other hand, indicate a change in the interlayer spacing and a potential decrease in crystallite size as a result of structural strain. These peak shifts demonstrate that the synthesis or treatment procedures applied to each cathode had an impact on the structural properties of MoS_2.

Fig. 6(c) shows the linear fitting plot of $\beta \cos(\theta)$ vs. $4 \sin(\theta)$, where the slope and intercept of the fitted line represent strain and crystallite size values, the values of strain ε and crystallite size D are listed in Table 3. During discharge, this analysis reveals a substantial the crystallite size decreases (indicating nano-crystallization or amorphization) while the strain increases, upon recharge, both parameters return to their initial values. This behavior confirms that the sulfur cathode lattice undergoes reversible volumetric contraction and expansion associated with the insertion and extraction of Na^+ ions within the sulfur framework. After recharging, the pattern indicates partial recovery of crystalline sulfur peaks at $\sim$23° and 28°, although they remain broader and less intense compared to the pristine cathode. The Scherrer equation applied to these broadened peaks reveals smaller crystallite sizes than in the pristine state, and Williamson–Hall plots indicate persistent lattice strain.[21] MoS_2 and SiC peaks remain relatively stable throughout the cycling process, confirming their structural robustness and potential role in buffering stress and facilitating electron/ion transport. The super carbon remains X-ray amorphous, contributing to the background without identifiable peaks.

In conclusion, XRD analysis supported by Scherrer and Williamson–Hall calculations demonstrates significant structural evolution of the S/MoS_2/SiC/super carbon cathode during cycling. While sulfur undergoes size reduction and increased strain during discharge with partial recovery upon charge, the stability of MoS_2 and SiC phases enhances the mechanical integrity and cycle stability of the electrode. This underscores the importance of composite design for managing structural

Table 3 Strain and crystallite size of the cathode (S_0, S_1 and S_2) from W−H plot

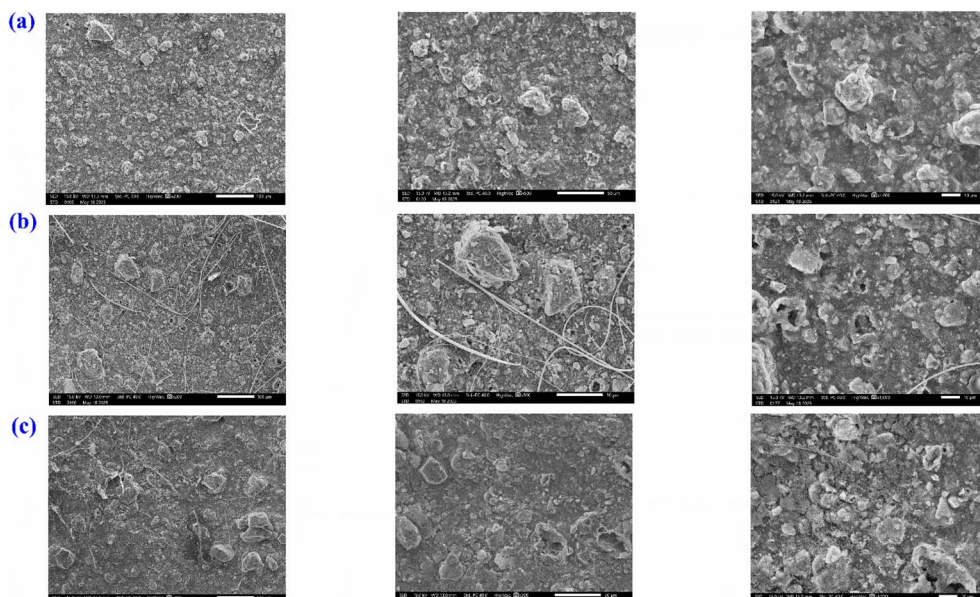| Element	S_0	S_1	S_2
Strain (ε) $\times 10^{-3}$	0.0648	0.850	0.267
Crystallite size D (nm)	55.91	47.48	64.65

Fig. 7 SEM of S-cathode extracted from Na‖NaPF$_6$‖Mo@Si@S full cell. (a) S$_0$, (b) S$_1$ and (c) S$_2$.

dynamics and improving Na/S battery performance.[22] In Fig. 7(a–c) SEM images of the sulfur (S) cathode in a Na/S battery are shown under three electrochemical states (a) pristine, (b) discharged, and (c) discharged/charged at three increasing magnifications (left to right) are denoted as S$_0$, S$_1$, and S$_2$, respectively. At the pristine state (a), the surface morphology across all magnifications appears relatively smooth and compact, with uniformly dispersed sulfur particles. At higher magnifications, the sulfur particles show well-defined crystalline edges and minimal porosity, indicating a structurally intact cathode with little to no prior electrochemical degradation. In the discharged state (b), the surface becomes rougher and more irregular. At low magnification, cracks and loose aggregates are visible, suggesting structural disintegration due to the formation of Na$_2$S and Na-polysulfides. With increasing magnification, these features become clearer, the sulfur particles exhibit a granular, porous morphology, and the surface shows signs of volume expansion and intermediate deposition, characteristic of the discharge process. At the discharged/charged state (c), partial restoration of the cathode surface is observed. At low magnification, the film appears less compact than the pristine sample, with the emergence of fibrous or wire-like structures likely residual reaction products or conductive additives reoriented during cycling. At medium and high magnification, these structures intertwine with residual sulfur particles, indicating incomplete reversibility. Despite some surface recovery, persistent porosity and morphological heterogeneity suggest side reactions and irreversible changes impacting long-term performance. The magnification-dependent SEM analysis highlights the dynamic microstructural evolution of the S cathode during cycling, emphasizing the need for material strategies that can accommodate volume change and improve reversibility in Na/S batteries.[23]

Conclusion

A multifunctional Mo@Si@S composite cathode was demonstrated as an effective strategy to enhance room-temperature sodium–sulfur battery performance by suppressing polysulfide shuttling, accelerating Na$_2$S$_x$ redox kinetics, and improving interfacial stability. The synergistic roles of polar MoS$_2$ and mechanically robust SiC enable diffusion-controlled Na$^+$ transport, reversible sulfur conversion, and improved cycling stability, particularly after short-term ambient storage. Nevertheless, rapid capacity fading in the early cycles and limited long-term capacity retention highlight persistent challenges related to sulfur utilization, electrolyte compatibility, and interfacial degradation. Based on the findings of this work, several targeted optimization directions can be identified for future studies. These include fine-tuning the MoS$_2$/SiC ratio to balance catalytic activity with mechanical buffering, optimizing electrolyte formulations to suppress parasitic reactions and stabilize electrode–electrolyte interfaces, and applying interface engineering strategies such as surface modification or binder optimization to improve sulfur retention and long-term cycling stability. Together, these approaches provide feasible pathways to translate the high initial activity of MoS$_2$–SiC-based cathodes into more durable room-temperature Na–S battery systems.

Conflicts of interest

The authors declare no competing interests.

Data availability

This data is available from the authors upon reasonable request.

Acknowledgements

References

1 J. Zhou, Y. Yang, Y. Zhang, S. Duan, X. Zhou, W. Sun and S. Xu, *Angew. Chem., Int. Ed.*, 2021, **60**, 10129–10136.

2 S. Luo, J. Ruan, Y. Wang, J. Hu, Y. Song, M. Chen and L. Wu, *Small*, 2021, **17**, 2101879.

3 H. Wan, L. Cai, Y. Yao, W. Weng, Y. Feng, J. P. Mwizerwa, G. Liu, Y. Yu and X. Yao, *Small*, 2020, **16**, 2001574.

4 Z. Huang, B. Song, H. Zhang, F. Feng, W. Zhang, K. Lu and Q. Chen, *Adv. Funct. Mater.*, 2021, **31**, 2100666.

5 H. Park, C. Jeon, S. Kansara, C. Lee, S. Xiong, Z. Sun and J.-Y. Hwang, *J. Power Sources*, 2026, **661**, 238587.

6 C. Qian, Z. Wang, D. Fu, A. Li, J. Xu, L. Shen, X. Wu and H. Li, *J. Power Sources*, 2024, **611**, 234759.

7 D. Su, D. Zhou, C. Wang and G. Wang, *Adv. Funct. Mater.*, 2018, **28**, 1800154.

8 X. Zhong, Y. Huang, J. Cai, Y. Li, Z. He, D. Cai, Z. Geng, W. Deng, G. Zou and H. Hou, *J. Am. Chem. Soc.*, 2024, **146**, 32124–32134.

9 H. Zhang, Y. Bai, W. Sun, X. Yang, R. Ma, L. Dai and C. M. Li, *ACS Nano*, 2025, **19**, 9081–9095.

10 Y. Wu, Q. Xu, L. Huang, B. Huang, P. Hu, F. Xiao and N. Li, *J. Colloid Interface Sci.*, 2024, **654**, 649–659.

11 Y. Wu, Q. Xu, L. Huang, B. Huang, P. Hu, F. Xiao and N. Li, *J. Colloid Interface Sci.*, 2024, **654**, 649–659.

12 H. Shu, F. Li, C. Hu, P. Liang, D. Cao and X. Chen, *Nanoscale*, 2016, **8**, 2918–2926.

13 Y. He, Z. Chang, S. Wu and H. Zhou, *J. Mater. Chem. A*, 2018, **6**, 6155–6182.

14 S. A. Mahmood, N. N. Mobarak, M. F. Shibl and K. A. Soliman, *Mater. Chem. Phys.*, 2025, **332**, 130236.

15 A. D. Bimonugroho, Design and Synthesis of Advanced Anode Materials for Next-Generation Sodium-Ion Batteries, PhD thesis, Seoul National University, 2024.

16 X. Xu, D. Zhou, X. Qin, K. Lin, F. Kang, B. Li, D. Shanmukaraj, T. Rojo, M. Armand and G. Wang, *Nat. Commun.*, 2018, **9**, 3870.

17 L. Zhou, O. Ragab, N. Wally, K. F. Qasim, X. Li, M. El-Desoky, W. Xing and E. Sheha, *RSC Adv.*, 2024, **14**, 37902–37910.

18 J. Kim, S. K. Mohanty and H. D. Yoo, *J. Appl. Electrochem.*, 2021, **51**, 703–713.

19 A. P. Nowak, P. Rutecki, M. Szkoda and K. Trzciński, *Energies*, 2024, **17**, 3233.

20 C. Jeans, *Geol. Mag.*, 1998, **135**, 819–842.

21 E. L. Gray, J.-I. Lee, Z. Li, J. Moloney, Z. J. Yang and M. Chhowalla, *ACS Nano*, 2025, **19**, 8939–8947.

22 B. Zhang, X. Qin, G. Li and X. Gao, *Energy Environ. Sci.*, 2010, **3**, 1531–1537.

23 X. Yu and A. Manthiram, *Chem.–Eur. J.*, 2015, **21**, 4233–4237.